Article

Evaluation of the Continuous Wavelet Transform for Detection of Single-Point Rub in Aeroderivative Gas Turbines with Accelerometers

Alejandro Silva [1*], Alejandro Zarzo [1†], Juan M. Muñoz-Guijosa [2] and Francesco Miniello [3]

[1] Department of Applied Mathematics, Escuela Técnica Superior de Ingenieros Industriales, Universidad Politécnica de Madrid, Calle de José Gutiérrez Abascal 2, 28006 Madrid, Spain.
[2] Department of Mechanical Engineering, Escuela Técnica Superior de Ingenieros Industriales, Universidad Politécnica de Madrid, Calle de José Gutiérrez Abascal 2, 28006 Madrid, Spain.
[3] Baker Hughes, a GE Company – Bently Nevada, Calle Josefa Valcárcel 26, 28027 Madrid, Spain.
[*] First author: a.silvab@alumnos.upm.es; Phone: +34 687 044 632.
[†] Corresponding author: alejandro.zarzo@upm.es; Phone: +34 626 517 594

Abstract: A common fault in turbomachinery is rotor–casing rub. Shaft vibration, measured with proximity probes, is the most powerful indicator of rotor-stator rub. However, in machines such as aeroderivative turbines, with increasing industrial relevance in power generation, constructive reasons prevent the use of those sensors, being only acceleration signals at selected casing locations available. This implies several shortcomings in the characterization of the machinery condition, associated with a lower information content about the machine dynamics. In this work we evaluate the performance of the Continuous Wavelet Transform to isolate the accelerometer signal features that characterize rotor–casing rub in an aeroderivative turbine. The evaluation is carried out on a novel rotor model of a rotor-flexible casing system. Due to damped transients and other short-lived features that rub induces in the signals, the Continuous Wavelet Transform proves being more effective than both Fourier and Cepstrum Analysis. This creates the chance for enabling early fault diagnosis of rub before it may cause machine shutdown or damage.

Keywords: machine fault diagnosis; rotordynamics; rub; aeroderivative turbines; accelerometers; early fault detection; fourier analysis; real cepstrum; continuous wavelet transform

1. Introduction

The flawless operation of rotating machinery such as turbomachines plays a key role in many branches of Industry such as electrical power and heat generation, aerospace and naval propulsion, and manufacturing. As their performance levels have risen steadily in the course of time their margins of admissible operation have shrunk. A failure in any of these machines could cause considerable economical or even human losses. So, it becomes convenient to put in place a maintenance program which allows to detect any abnormality in the machinery operation at the early stages, before a fault at an advance stage forced it to be put out of duty.

In a turbomachine a *rotor* transmits the mechanical power to or from an external power source or sink. The rotor contains circumferential arrangements of *blades* called *disks* attached to a rotating *shaft*. A *casing* built around the rotor sustains it and channels the working fluid passing through the machine with the aid of disks of *vanes* (Figure 1). Optimal thermodynamical efficiency requires, among many other factors, most of the working fluid flow passing through the rotor blades with no leaks. To achieve this the diametrical clearance between the rotor and the *seals* contained by the casing must be minimized, but the price to pay is a higher probability of rotor–casing rub. This phenomenon causes, when unnoticed, wear and overheating and, if severe, may be highly destructive. Even if modern industrial equipment counts with machine protection relays that shut the machine down in case of faulty or abnormal duty, a better knowledge of the dynamics of faulty machines—in this case, rotor–casing rub—and more effective monitoring and protection systems lead to earlier diagnosis, shorter downtimes and lower operation and maintenance costs.

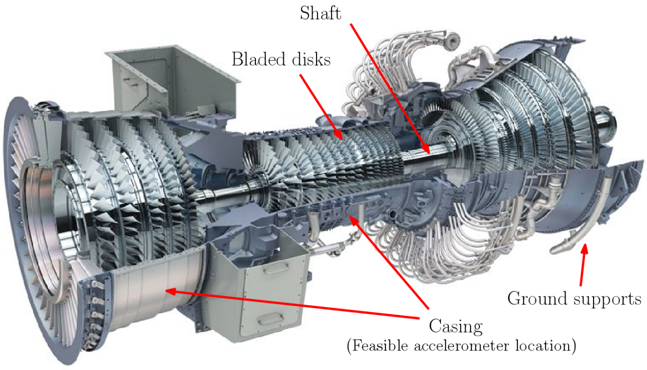

Figure 1. Cutaway of an aeroderivative gas turbine and main parts -from https://www.power-eng.com-.

Rub dynamics, monitorization, detection and diagnosis or rub and other malfunctions have been research topics in the Academia during the last decades and the Industry has large experience on the matter [1,2]. Rotor vibration is the most common indicator of rub available for monitorization. In most gas and steam turbines vibration is measured with proximity sensors mounted between the rotor and stator. In classes of turbomachinery such as in aeroderivative gas turbines—an elementary part of heat and power co-generation processes, combined-cycle power plants, oil and gas processing and marine propulsion—those sensors cannot be fitted for a number of design issues: the very low shaft–bearing relative deformations derived from the use of ball or rolling bearings instead of journal bearings, and the increased difficulty to fulfill the maintenance needs of these sensors. Leveraging on the high casing flexibility of aeroderivative turbines, its operation can instead be monitored by means of indirect vibration measurement techniques such as accelerometers mounted on the casing (Figure 2).

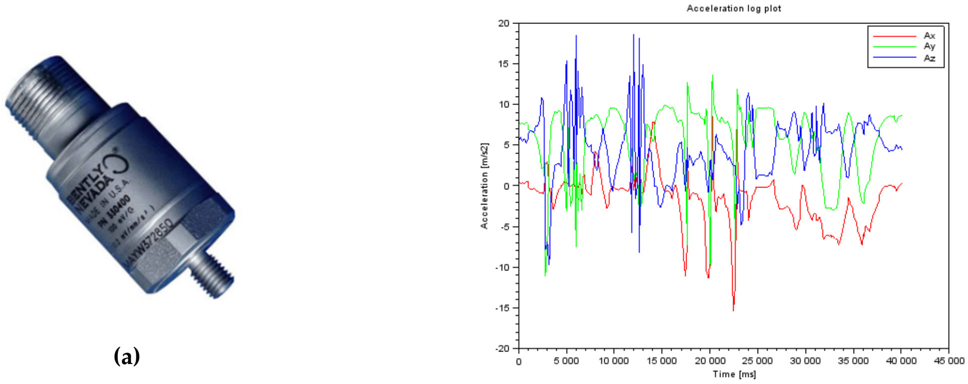

(a)

(b)

Figure 2. (a) GE's Bently Nevada 330400 Sensor: accelerometer for casing acceleration measurement—from GE Measurement & Control: https://www.gemeasurement.com—. (b) Accelerometer output: acceleration as a function of time—from http://www.realglitch.com/—.

However, despite the industrial relevance of the problem, only a handful of papers have been published on the subject of the detection of rub with acceleration sensors on casing. The autors of [3–5] show the results of a series of experimental tests on an experimental aero-engine with a bladed disk and a casing that encloses it. Blades and casing rub with each other when the latter is squeezed onto one of the rotating disk by turning one or several screws. This rub is continuous over some or all of the disc blades in one or several fixed points of the casing. Obviously, if all disk blades rub, the number of impacts per cycle of rotation in each rub point is equal to the number of blades. Casing acceleration is measured on a set of points with accelerometers and spectral analysis is conducted on the data. Raw data and its analysis show periodic rotor–casing impacts taking place with frequency equal to the product of the rotating speed with the number of blades. These impacts have an amplitude-modulated component with frequency equal to rotation speed. Chen [6] contrasts those experimental results with a simulation in a rotor model described in [7]: the shaft is discretized into beam elements, the disk blades are solid—undeformabl—straight beams and the casing is modeled as a two-dimensional curved non-rotating beam with two displacements on the radial plane per node. Wang [8] another experimental rig is used to reproduce the same type of rub than in the previous papers: rub is inflicted by means of a nylon block on the casing that impacts with a number of disc blades as the shaft rotates. The data spectra also highlight the impact-frequency peak and the impact modulation, as well as a rotation-frequency amplitude peak and its super-synchronous multiples, clearly seen in the low-frequency spectrum band.

The publications cited in the previous paragraph are centered on the same type of rub: with the infliction of a massive relative rotor–casing mechanical deformation on one or several fixed points, or by fitting an obstacle between rotor and casing, the authors reproduce a rub that extends through all or almost all the circumferential rotor disk blades. There is an interest for the study of lighter and more frequent types of rub such as partial, single-point rub [23]: one rotor spot impacting a single point on the casing (Figure 3). At the same time, there is an opportunity to study the dynamics of longer, flexible casings in medium or heavy-duty turbomachinery and the influence of the axial positions of casing sensors and rub points on the collected signals. The latter could be attained with the construction of larger experimental rotor–casing rigs and their modelization as three-dimensional shells instead of using curved beams on the radial plane. Our research is centered on aeroderivative machines, whose rotating speeds during steady-state regime use to lie between the first and second rotor critical speeds, far lower than the regimes of most aero-engines. In most cases reported by the Industry rotor–casing rub leading to rotor shutdown took over in that regime. This research focuses on the identification of possible rub in the duty range of aeroderivative turbines. Any rub regime in a rotating machine is, in the onset, a light rub whose severity may increase in time if no measure is taken, therefore the best signal processing tools use in the task of diagnosing rub should be well suited to the lightest rub that can be measured and detected. Knowledge of the consequences of the lightest types of rotor–casing rub on machine dynamics and vibration is necessary to be able to detect it and take corrective action as soon as possible. With early diagnosis further damage can be prevented and maintenance programs and operation costs can be optimized.

In this work, the performances of the Fourier Transform and the Cepstrum [9], the standard tools used by the Industry for the monitorization and diagnosis of malfunctions in machinery, are compared to the performance of the Continuous Wavelet Transform [10] for the detection of single-point rub in aeroderivative turbines. Wavelet Analysis has been extensively used in machine fault diagnosis as [11] shows and therefore is a promising alternative to the traditional machine diagnosis methods. To do so, a novel rotor model with flexible casing and supports, presented in section 2, has been developed. With this model we carried out the simulation of a rotating machine subject to rotor unbalance and rotor–casing rub. This model is able to reproduce many types, conditions and severities of rub but the results described here revolve around single-point rub—The most common type of rub diagnosed in turbomachinery, see Figure 3—. The results of those simulations are described in section 3: the model equations were integrated and vectors of casing acceleration and velocity samples—or *time records*—were extracted and processed with the methods cited above. The performance of the three signal processing methods can be measured by the degree of rub features that each method can isolate,

Peer-reviewed version available at Sensors 2018, 18, 1931; doi:10.3390/s18061931

the computational resources they consume, and by the time necessary to identify rub features on the signals since the onset of a rub condition in the machine. In the presence of rub the time-domain acceleration signals consist of trains of impulses followed by oscillating transients that contain damped rotor and casing vibration. All those features in both low and high-frequency bands may be visible to the Fourier spectra and the cepstra only if the sampling times are large enough, but the Continuous Wavelet Transform proves being able to highlight and localize these features in a short sampling vector containing just a few rotor–casing impacts, confirming the existence of a periodical impact on the casing. This work goes in the direction to find tools that allow for rub diagnosis while its severity it still very small in order to prevent machine damage or fault—early fault diagnosis—.

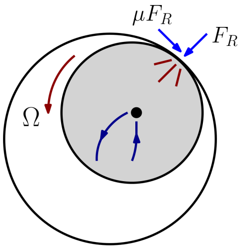

Figure 3. Single-point rotor–casing rub. One rotor spot impacts one point on the casing at a time. During the contact, normal and friction rub forces—light blue—change the rotor orbit direction—dark blue—and inflict vibration in the system.

2. Materials and Methods

The models, simulations and algorithms described here have been implemented in Matlab 2017a.

2.1. Rotor-casing model

The rotor-flexible casing model that has been developed (Figure 4) comprises a cylindrical shaft—S, blue color—with a number of cylindrical rigid solid disks—D_1 and D_2, red color—attached to it. Together they form the machine rotor, which rotates at a constant speed Ω. The rotor is supported on bearings—B_1 and B_2, violet—that are radially bound to the cylindrical shell that forms the machine casing—C, black—. The bearing-casing joints are modeled as very stiff bar trusses between each bearing and a number of homogeneously-distributed points in the casing—BC_1, not represented for simplicity; and BC_2, yellow—. All components are modeled under the hypotheses of linear elasticity —with the exception of the rigid solid disks—, homogeneity and small displacements and deformations. Any of the two shaft extremes may incorporate a linear elastic coupling attached to the ground at the other side—*coupl*, dark blue—. The casing rests on the ground through linearly elastic supports attached to several points of the casing—CF_4, not represented; CF_1, CF_2 and CF_3, black—. The z axis of the global cartesian reference system—black—follows the rotor axial direction and the axes x and y are contained on a rotor radial plane at one of the shaft extremes. A positive rotor rotation speed follows the shortest path from x to y.

This rotor may vibrate due to the action of unbalance and rub forces that will be described further below. The motions caused by those forces are measured by one or several accelerometers on the casing—green—which yield casing acceleration versus time. The rotor radial motion—called the rotor *orbit*—is also of great interest because that vibration is what is monitored in conventional turbomachines as the indicator of malfunction.

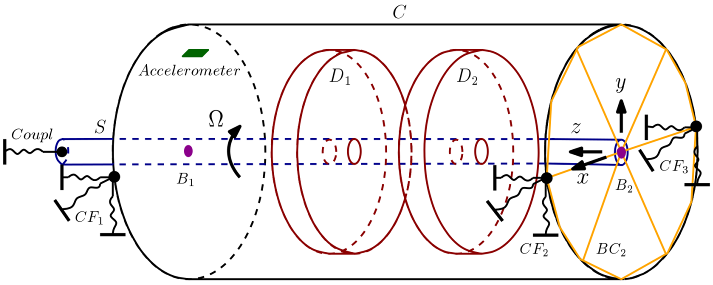

Figure 4. The rotor-flexible casing model.

This model can be adapted to any material properties, dimensions and numbers of disks, bearings and supports, as long as the model hypotheses hold. As in Figure 4, our model has been set up with two disks, two rotor bearing supports on both casing sides, a coupling at one of the shaft extremes and four casing-ground supports attached to the casing ends on a plane that splits the casing in two identical halves. Shaft and disks are made of steel. The casing's material is carbon fiber. Bearing-casing joints are modeled as very rigid elements so that most of the bearing-casing union elasticity rests on the bearings themselves. The most remarkable dimensions and mechanical properties of the model are shown in Table 1. These values of Table 1 are within the range of those appearing in some reduced scale experimental devices typically employed in the literature for model validation [6,12].

Table 1. Rotor-casing model dimensions and mechanical properties.

Shaft length:	$0.6\ m$	Young modulus of shaft:	$2 \cdot 10^{11}\ Pa$
Distance between shaft bearings:	$0.4\ m$	Shaft density:	$7850\ kg\ m^{-}3$
Shaft diameter:	$0.01\ m$	Casing density:	$1600\ kg\ m^{-3}$
Disk mass:	$1.5\ kg$	Young modulus of casing:	$7 \cdot 10^{10}\ Pa$
Disk thickness:	$0.025\ m$	Poisson's ratio of casing:	0.1
Disk diameter:	$0.1\ m$	Bearing radial direct stiffness:	$1 \cdot 10^{8}\ N\ m^{-1}$
Casing midplane diameter:	$0.134\ m$	Casing support stiffness:	$5 \cdot 10^{5}\ N\ m^{-1}$
Casing length:	$0.4\ m$	Bearing-casing truss bar stiffness:	$1 \cdot 10^{12}\ N\ m^{-1}$
Casing thickness:	$0.003\ m$	Bearing mass:	$0.02\ kg$

The model simulation requires the dynamical system of ordinary differencial equations—SODE—shown in 1. In this work it has been derived with the Finite-Element Method following the model hypotheses. A thin, slender shaft has been discretized into two-node Euler-Bernuolli beam elements with five degrees of freedom per node—three translations and two bending rotations—following [13]. The rigid solid disks—modeled as in [14]—share these five degrees of freedom with the shaft. The casing was split into a grid of equally-sized Mindlin-Reissner shell elements with four nodes at the element corners and two additional nodes on the radial boundaries to allow the isoparametric modeling of a curved cylindrical shell. The formulation we followed to derive the local equations of casing elements is in [15] and is based on treating each shell element as a degenerate 3D element under shell hypotheses, with nodes only in the midplane. Each casing node has five degrees of freedom: the three cartesian translations and two bending rotations around the in-plane local axes, as usual in shell elements. The bearing nodes and those of the stiff bars that bind them to the casing only have as degrees of freedom the three translations in space. As bearing hypotheses, there are no cross-coupled reaction forces between bearings and shaft and the shaft is supposed to rotate freely in the bearing, with no reaction forces caused by relative bearing-shaft angular deformations. This hypotheses are applicable when the shaft is supported on ball or roller bearings, as it is in most aeroderivative turbines.

Peer-reviewed version available at Sensors 2018, 18, 1931; doi:10.3390/s18061931

$$\mathbf{M}\mathbf{u}'' + (\mathbf{C} + \Omega\mathbf{G})\mathbf{u}' + \mathbf{K}\mathbf{u} = \mathbf{F_U}(t) + \mathbf{F_R}(\mathbf{u}, \mathbf{u}') \tag{1}$$

M, **C**, **G** and **K** are the mass, viscous damping, gyroscopic and stiffness matrices respectively. These global matrices are assemblies of the local matrices of shaft and disk—*S+D*—, casing—*C*—and bearings—*B*—:

$$\mathbf{M} = \begin{pmatrix} \mathbf{M_{S+D}} & & \\ & \mathbf{M_C} & \\ & & \mathbf{M_B} \end{pmatrix} \quad \mathbf{G} = \begin{pmatrix} \mathbf{G_{S+D}} & & \\ & \mathbf{0} & \\ & & \mathbf{0} \end{pmatrix} \quad \mathbf{C} = \begin{pmatrix} \mathbf{C_{S+D}} & & \\ & \mathbf{C_C} & \\ & & \mathbf{C_B} \end{pmatrix} \quad \mathbf{K} = \begin{pmatrix} \mathbf{K_{S+D}} & & \\ & \mathbf{K_C} & \\ & & \mathbf{K_B} \end{pmatrix}.$$

u, **u**′ and **u**″ are the vector of node displacements and its time derivatives: velocity and acceleration. Analogously to the matrices, these vectors are assemblies of local vectors of shaft, casing and bearing displacements, each with its own degrees of freedom:

$$\mathbf{u} = (\mathbf{u_{S+D}} | \mathbf{u_C} | \mathbf{u_B})^T = (\mathbf{u}_1\ \mathbf{u}_2\ ...\ \mathbf{u}_N)^T.$$

Simulations were carried out with a mesh of 19 shaft nodes—18 shaft beam elements—, two bearing nodes and 5490 casing nodes—2700 casing shell elements—. The first step was a modal analysis of the free undamped system with $\Omega = 0$. The first rotor and casing modes of vibration and their corresponding undamped natural frequencies are shown on Figure 5.

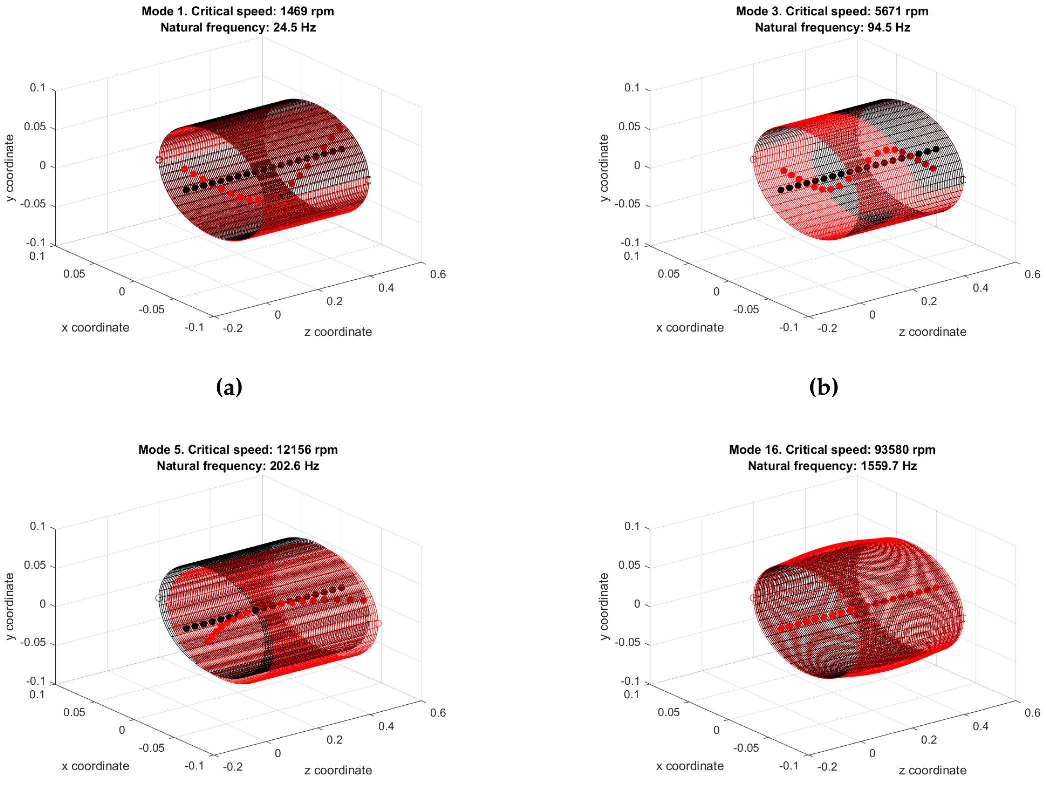

(a) (b) (c) (d)

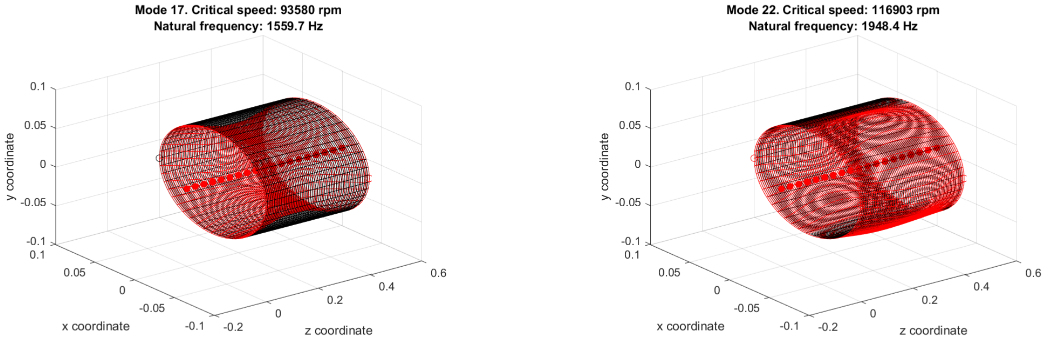

(e) **(f)**

Figure 5. Lowest shaft and casing natural modes. (a) Rotor bending mode with one antinode. (b) Rotor bending mode with two antinodes (c) Casing rigid solid mode with shaft deflection. (d) Lowest casing longitudinal mode. (e) and (f) Lowest casing flexural modes.

Following [7], the system has been hypothesized to have a Rayleigh damping: the global viscous damping matrix **C** as a linear combination of the mass and stiffness matrix:

$$\mathbf{C} = C_M\mathbf{M} + C_K\mathbf{K}.$$

The two constants C_M and C_K are the result of solving a two-variable system of equations given two system natural frequencies $\omega_{N,1}$ and $\omega_{N,2}$ with known damping factors $\xi_{d,1}$ and $\xi_{d,2}$:

$$\xi_{d,i} = \frac{1}{2}\left(\frac{C_M}{\omega_{N,i}} + C_K\omega_{N,i}\right),\ i = 1,2.$$

The variation of natural frequencies with rotation speed in the damped free rotor-flexible casing due to the speed-variable damping term of equation 1 is represented on the *Campbell diagram* shown in Figure 6.

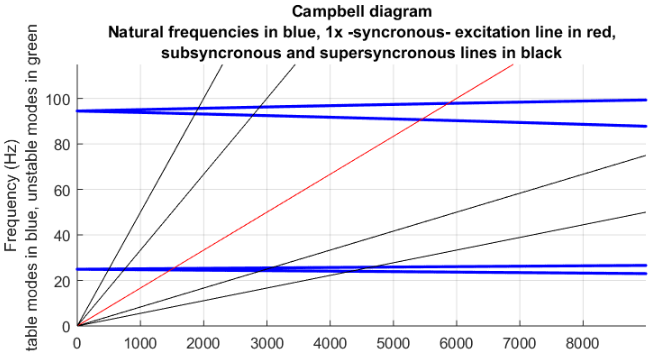

Figure 6. Campbell diagram of the two first rotor natural modes. The two bending modes split with increasing rotation speed due to the gyroscopic effect. The intersections of the 1x line with the natural modes mark the *resonance* or *critical* speeds of the rotor. All the represented modes are stable.

Peer-reviewed version available at *Sensors* **2018**, *18*, 1931; doi:10.3390/s18061931

2.1.1. Rotor unbalance

The most common source of excitation in a rotating machine is an unbalance force in the rotor [16]. The unbalance force vector in shaft node i is:

$$\mathbf{F}_{\mathbf{U},i} = M_{U,i}\Omega^2 r_{U,i}(\cos{(\Omega t - \psi_{U,i})}\ \sin{(\Omega t - \psi_{U,i})}\ 0\ 0\ 0)^T,$$

where $M_{U,i}$ is an unbalance mass, $r_{U,i}$ is the distance between the unbalance mass and the rotation axis and $\psi_{U,i}$ is a phase angle that defines the angular position of the unbalance mass with respect to a reference point on the rotor—in rotating machines this reference may be the *keyphasor* mark, see [17]—-.

2.1.2. Rub forces

A number of rotor–casing rubs can be defined, each between a casing node and a rotor node (Figure 7). An obstacle with stiffness and damping coefficients k_R and c_R is fitted on the casing node j. This obstacle may impact the rotor on node i. When the system is at rest the clearance between rotor and obstacle is ϵ. If the rotor–casing relative deformation becomes larger than ϵ two forces appear in the system: a normal, viscoelastic force F_R and a tangential friction force proportional to the normal rub force by a friction coefficient μ that has been considered constant for any relative rub velocity between rotor and obstacle. If the obstacle contact surface is flat and parallel to the casing at the attachment node j its normal unitary vector equals the casing unitary normal vector at j, $\mathbf{v}_{2,j}$.

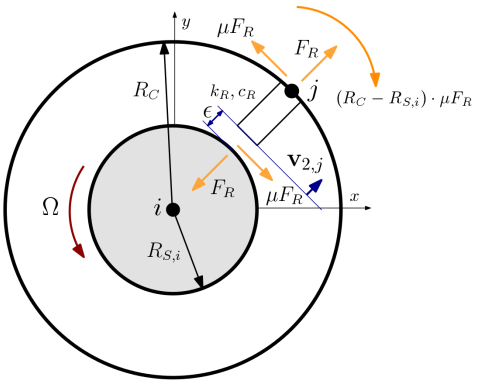

Figure 7. Rub model and forces on shaft and casing nodes.

The relative displacement d_R between rotor and obstacle and the relative velocity d'_R can be expressed as:

$$\begin{aligned} d_R &= \langle (u_{x,j} - u_{x,i}\ u_{y,j} - u_{y,i}),\ \mathbf{v}_{2,j}\rangle - \epsilon \\ d'_R &= \langle (u'_{x,j} - u'_{x,i}\ u'_{y,j} - u'_{y,i}),\ \mathbf{v}_{2,j}\rangle, \end{aligned}$$

being $u_{x,j}$, $u_{y,j}$, $u_{y,i}$ and $u_{x,i}$ the radial displacements of the casing and rotor nodes respectively. $u'_{x,j}$, $u'_{x,i}$, $u'_{y,j}$ and $u'_{y,i}$ are node velocities. $\langle .,\ .\rangle$ is the notation for the inner product of two vectors.

The rub normal force results from the product of relative displacements and velocities with stiffness and damping contact coefficients k_R and c_R and a Heaviside function that equals one when the relative deformation is larger than the clearance ϵ, and zero otherwise:

$$F_R(\mathbf{u},\ \mathbf{u}') = (k_R d_R + c_R d'_R) \cdot H(d_R - \epsilon).$$

The direction of the rub friction vector depends on the direction of relative displacement between the rotor and the rubbing obstacle. This is given by the sign of the relative rotor–casing rub velocity, defined as:

$$v_{RC} = R_{s,i} \cdot \Omega + \langle (u'_{x,j} - u'_{x,i} \; u'_{y,j} - u'_{y,i}),\ (\sin\gamma \; - \cos\gamma)^T \rangle + u'_{\Phi_\xi,j} \cdot (R_c - R_{s,i}),$$

where γ is the angle of $\mathbf{v}_{2,j}$ with respect to x, and $u'_{\theta_{\xi,j}}$ is the casing z-axis bending velocity at node j.

Since the rub spot stands at a distance $R_c - R_{s,i}$ of the casing node, the friction force on the rub spot inflicts, by balance of forces, a bending moment on the casing around the z axis. Normal and friction rub forces on rotor and casing are projected on the global coordinate axes, resulting in the following local rub vectors of rotor—node i—and casing—node j—:

$$\mathbf{F}_{\mathbf{R},i}(\mathbf{u},\mathbf{u}') = F_R \begin{pmatrix} -\cos\gamma \\ -\sin\gamma \\ 0 \\ 0 \\ 0 \end{pmatrix} + \mu \cdot sign(v_{RC}) \cdot F_R \begin{pmatrix} \sin\gamma \\ -\cos\gamma \\ 0 \\ 0 \\ 0 \end{pmatrix}$$

$$\mathbf{F}_{\mathbf{R},j}(\mathbf{u},\mathbf{u}') = F_R \begin{pmatrix} \cos\gamma \\ \sin\gamma \\ 0 \\ 0 \\ 0 \end{pmatrix} + \mu \cdot sign(v_{RC}) \cdot F_R \begin{pmatrix} -\sin\gamma \\ \cos\gamma \\ 0 \\ -(R_c - R_{s,i}) \\ 0 \end{pmatrix}.$$

2.2. *Model reduction and integration*

2.2.1. The Craig-Bampton method

The model mesh counts with a total of 27551 degrees of freedom, making a numerical integration of model equation 1 too complicated for the limited speed and storage available and the large size of the integration output. Before its numerical integration the system should be reduced in size. This can be attained with the Craig-Bampton method [18]. As *boundary* degrees of freedom we choose those of the shaft, casing degrees of freedom affected by rub and degrees of freedom selected as data source for the measurement of casing acceleration. The remaining degrees of freedom, known as *interior* degrees of freedom, are projected on a subspace whose basis is formed by the first 200 normal modes of a system with constrained boundary degrees of freedom.

The resulting system, with reduced matrices and force vectors $\mathbf{M_{CB}}$, $\mathbf{C_{CB}}$, $\mathbf{G_{CB}}$, $\mathbf{K_{CB}}$, $\mathbf{F_{CB,U}}$, $\mathbf{F_{CB,R}}$ and $\mathbf{F_{CB,M}}$, has only 300 degrees of freedom, a size a modern desktop computer can cope with in terms of storage and speed.

2.2.2. The Newmark-β methbd

For the numerical integration of the reduced system of equations we chose the implicit Newmark-β method [19]. This method uses, in an iterative fashion, a implicit finite-difference expression to calculate the velocities and displacements of time step $i+1$ from the displacements, velocities and accelerations of the former step i and the accelerations of the current step $i+1$. The Newmark-β method is for application to linear dynamical systems, but equation 1 contains a strongly nonlinear force term $\mathbf{F_R}$. This problem can be circumvented with the use of nonlinear algebraic solvers to clear the $i+1$th step velocities and displacements contained in the force term but a much simpler alternative is to substitute

Peer-reviewed version available at *Sensors* **2018**, *18*, 1931; doi:10.3390/s18061931

the state vector $(\mathbf{u}, \mathbf{u}')$ of the rub force term for the displacements and velocities calculated in the previous ith step:

$$\mathbf{F}_{\mathbf{R},\mathbf{CB}}(\mathbf{u}_{i+1}, \mathbf{u}'_{i+1}) \approx \mathbf{F}_{\mathbf{R},\mathbf{CB}}(\mathbf{u}_i, \mathbf{u}'_i).$$

2.3. *Signal extraction and processing*

2.3.1. Fourier Analysis

A vector $\mathbf{x}$ of periodical discrete signal samples with length N can be decomposed into a Fourier sum series with sinusoidal terms called *harmonics*. The N coefficients $\mathbf{X}(n)$ of the decomposition form the signal *spectrum* and are calculated with the *Discrete Fourier Transform*—DFT, more in [20]—. The sampling vector $\mathbf{x}$ contains, in this work, the radial acceleration of a casing node measured with respect to time, being T_s its sampling period. Before the spectrum calculation the signal is periodizised multiplying it element-wise with a Hamming window vector. If N is a power of two the *Fast Fourier Algorithm*—FFT, see [21]— is applicable, allowing for a much faster computation of the spectrum.

2.3.2. Real Cepstrum

The *cepstrum* [9], also known as the *spectrum of the spectrum* is a popular diagnosis tool in machinery condition monitoring. Generally, it is the inverse Fourier transform of the logarithm of a spectrum. In the case of the *Real Cepstrum* its mathematical definition is:

$$c(t) = \mathcal{F}^{-1}(\log|\mathcal{F}(x(t))|).$$

First, the complex phase information of the signal $x(t)$ is removed with the calculation of the module of its spectrum, $|\mathcal{F}(x(t))|$. Then the logarithm evens out the amplitude of any sidebands or impulse trains contained in the spectrum with the amplitudes of the main spectral components. After the application of the inverse Fourier transform, impulse trains and amplitude or frequency-modulated components contained in the original signal are highlighted in the resulting cepstrum and shown as periodical pulses called *rahmonics* with a time-dimensional periodicity called *quefrency*, measured in seconds.

2.3.3. Continuous Wavelet Transform

Analogously to the Continuous Fourier Transform—see [10]—the *Continuous Wavelet Transform*—CWT—is the inner product of a function $x(t)$ and a dilated and translated basis function $\Psi^*(\frac{t-b}{a})$ called *mother wavelet*:

$$W(a,b) = \langle x(t),\ \Psi_{a,b}(t)\rangle = \frac{1}{\sqrt{|a|}} \int_{-\infty}^{\infty} x(t) \cdot \Psi^*(\frac{t-b}{a})\, dt,$$

where a and b are, respectively, dilation and translation factors. The coefficient $W(a,b)$ gives a measure of the similarity between the function and the dilated and translated mother wavelet. The big advantage of the CWT over the Fourier Analysis is its potential for feature localization in both time and frequency domains, provided that the selected mother wavelet has good properties—smoothness, compact support, regularity, etc.—. Hence it is ideal for signals with a high content in transient components and irregularities that are invisible to the Fourier decomposition methods. CWT analysis with the Morlet function as the mother wavelet [32] has been successfully used as a tool for machine fault diagnosis in former studies [24–30].

3. Results

The simulated rotor–casing model comprises two disks symmetrically attached to the shaft. The second disk contains an unbalance mass M_U of $1.5 \cdot 10^{-3}$ kg at a distance r_U of $3.75 \cdot 10^{-2}$ m from the rotation axis with zero phase angle ψ_U. The viscous damping matrix has been estimated considering a damping factor of 0.04 and 0.06 at the critical speeds of 1500 and 5700 rpm respectively. A rub condition affects a shaft node close to one of the disks and one of the casing nodes in the same radial plane, with $k_R = 7.4 \cdot 10^6\ N\ m^{-1}$—two orders of magnitude larger than the shaft bending stiffness—, $c_R = 0$—no impact damping—and $\mu = 0.2$—Steel-to-steel rub—. The equation 1 is integrated with a time step of 2^{-17} s. Casing radial acceleration of a casing node close to one of the casing ends is extracted into a vector of 2^{18} samples at a rate of one sample per integration step, the sampling time of the collected acceleration data or *time record* being 2 s. The radial acceleration of casing node j, u''_j, as a casing accelerometer measures it is defined by its acceleration in the x and y degrees of freedom as $\sqrt{u''_{x,j} + u''_{y,j}}$.

It is common practice to integrate the accelerometer signals, monitoring velocity instead of acceleration with respect to time. The purpose is to attenuate the high-frequency noise contained in the accelerometer signal and to highlight the low-frequency band of the spectrum, which is the source of information that is most commonly used for protection purposes in rotating machinery [22]. Therefore a second sampling vector containing radial casing velocity, u'_j, is constructed from the simulation data. Rotor displacement orbits in the radial plane where is rubs the casing are also of interest because in conventional turbomachines rotor orbits are the preferred monitorization tool. Rotor orbits bring us confirmation of the existence of a rub in the simulated rotor-flexible casing model.

From the Campbell diagram (Figure 6) the first three rotor critical speeds are approximately 1500 rpm—corresponding to the rotor bending mode with one antinode—, 5400 and 5900 rpm—the bending mode with two antinodes—. The model has been simulated at a speed Ω of 3600 rpm—60 Hz—, between the first and the second critical speeds: the working range of a real aeroderivative machine. The purpose of selecting this rotation speed is to reproduce a rub condition that is observed very often in conventional turbomachines working at speeds above twice the first rotor critical speed: a single-point rub with one impact every two rotation cycles -see [23]-.

In Figures 8 and 9 we represent the rotor orbits, the full spectra of the rotor orbits [31] and casing acceleration and velocity plots of a rotor–casing model in steady-state regime under two conditions: no rub and light single-point rub. If there is no rub (Figure 8) the acceleration and velocity signals are dominated by a synchronous sinusoid resulting from the unbalance force excitation. If the clearance ϵ is small enough a stable single-point rotor–casing sets off, its intensity being of such magnitude so that the unbalance-related sinusoidal vibration is masked by new signal features resulting from the rub condition.

Every time the rotor impacts the casing two impulse peaks appear on the acceleration plot (Figure 9c): the first when rotor and casing come together, and the second when rotor and casing come apart, A transient that contains at most free high-frequency highly-damped vibration of rotor and casing precedes the first impulse. The high frequency of the free casing vibration during its contact with the rotor is closely related to the stiffening effect of the rub on the rotor system [23]. The second impulse at the rotor–casing split is then followed by the damped transitory corresponding to the 200 Hz casing rigid solid mode (Figure 5c). The number of rotor–casing impacts per second is half the rotation frequency: 30 Hz.

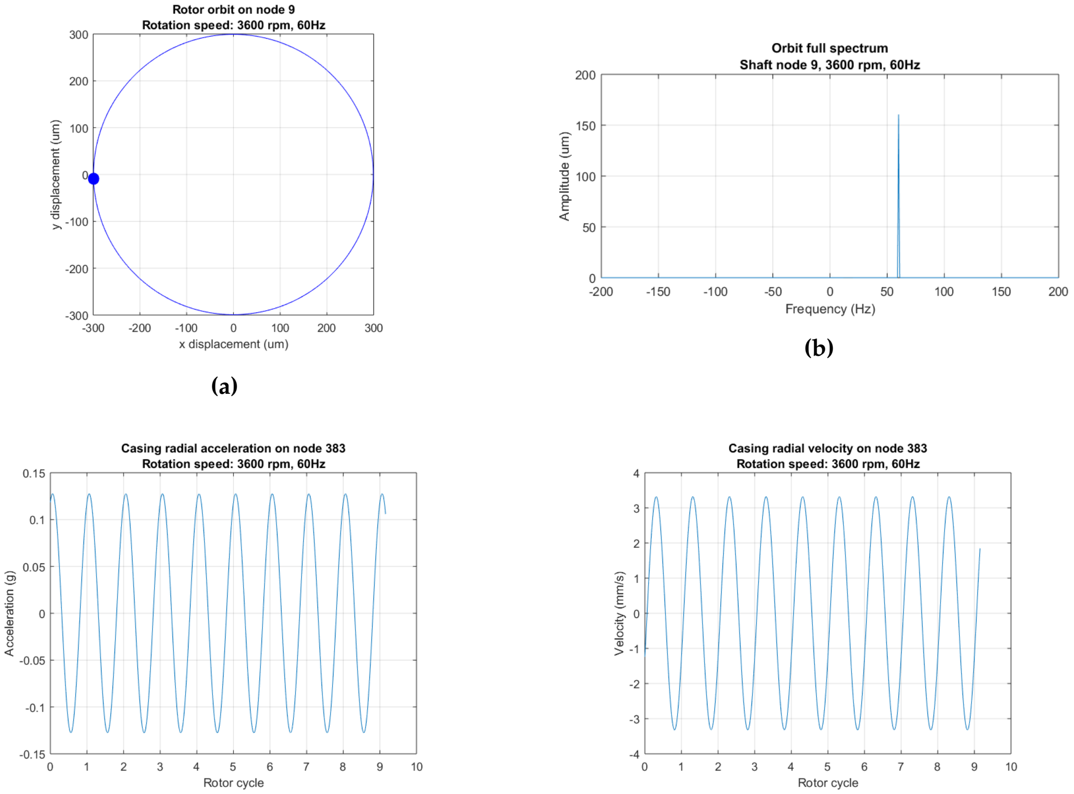

(a) **(b)**

(c) **(d)**

Figure 8. (**a**) Rotor orbit—shaft displacement on the radial plane—. (**b**) Full spectrum of the rotor orbit. (**c**) and (**d**) Acceleration versus rotor cycle—i.e. versus time—and velocity versus rotor cycle—'acceleration time plot' and 'velocity time plot' hereafter—measured on selected casing node at 3600 rpm. No rub. The shaft rotates in the anticlockwise direction.

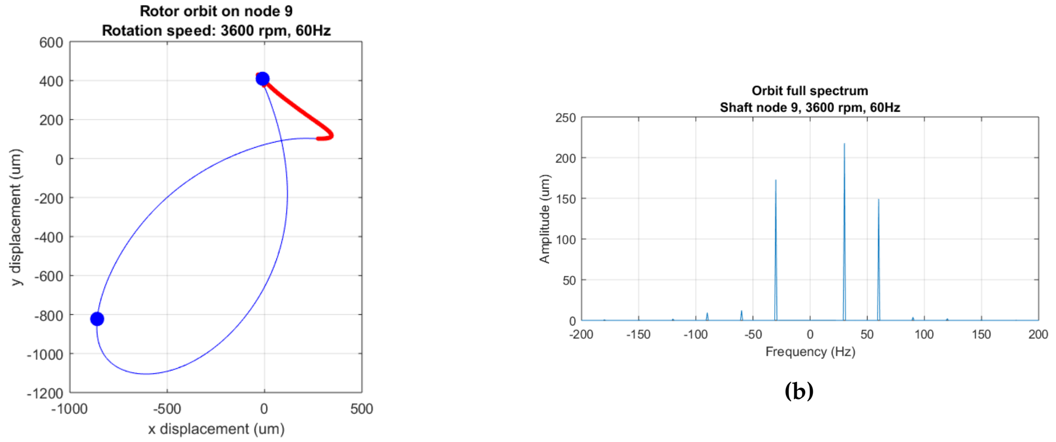

(a) **(b)**

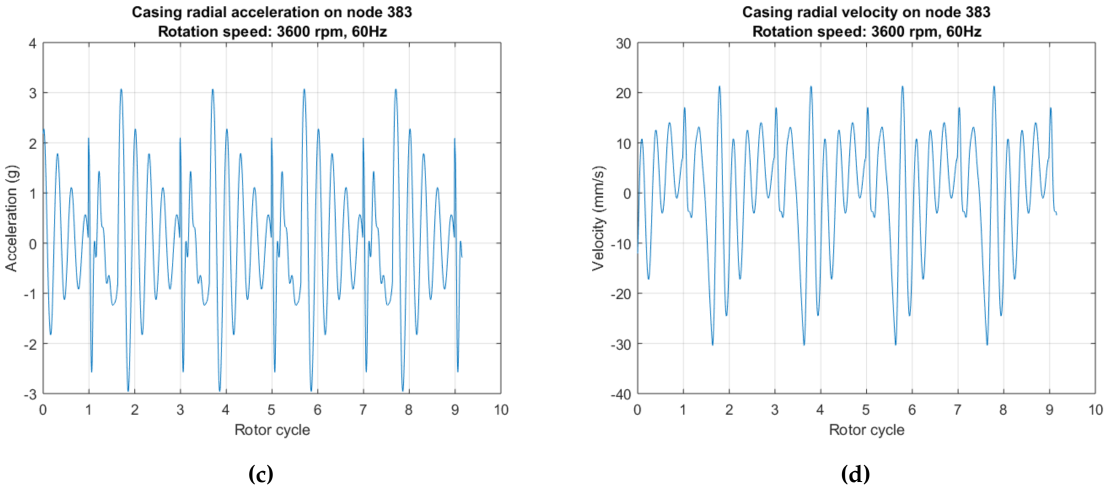

(c) **(d)**

Figure 9. (**a**) Rotor orbit, with the orbit segment where the rotor rubs the casing marked in red. (**b**) Full spectrum of the rotor orbit. (**c**) Acceleration time plot. (**d**) Velocity time plot. 3600 rpm. Light single-point rub ($\epsilon = 2.5 \cdot 10^{-4}\ m$). The shaft rotates in the anticlockwise direction.

A single-point rub regime is easy to identify on the Full Spectrum plots 9(b): it manifests itself as a pair of harmonics—forward and backward—with frequency half the rotation speed and equal or almost equal amplitude. This harmonic with half the rotation speed is a staple in the spectra of rubbing rotating machinery operating at speeds slightly above twice the first critical speed [23]. The construction of full spectra of rotor orbits requires the relative displacements between rotor and stator on at least one rotor radial plane. Unfortunately, that information cannot be collected in an aeroderivative turbine because of the technical challenge that means to fit proximity sensors in aeroderivative gas turbines.

In the following sections, the signal processing methods described above will be applied to the casing signals from the rotor with light rub (Figure 9) in order to isolate the signal features that allow for rub diagnosis.

3.0.1. Fourier Analysis

The Fourier spectra of the acceleration and velocity records under light single-point rub are shown in Figure 10. After an anti-alias filtering the acceleration data was downsampled to 28 kHz for a 14 kHz spectrum and the velocity data was downsampled to 2 kHz for a 1000 Hz spectrum. Then a Hamming windowing was applied to the new vectors of samples. The two sample records were two seconds long, hence the frequency resolution is 0.5 Hz. The two spectra are qualitatively very similar: each displays an impulse train with fundamental frequency equal to the rotor–casing impact frequency—half the rotation speed—, 30 Hz. The harmonics with the highest amplitude, apart from the fundamental harmonic in the velocity spectrum, are found in the 90–240 Hz band and are related to the excitation of the 200 Hz casing rigid solid vibration mode (Figure 5c).

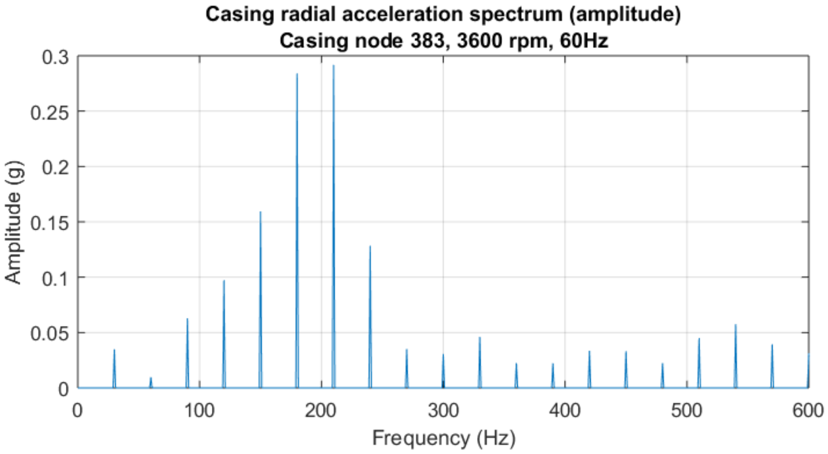

(a)

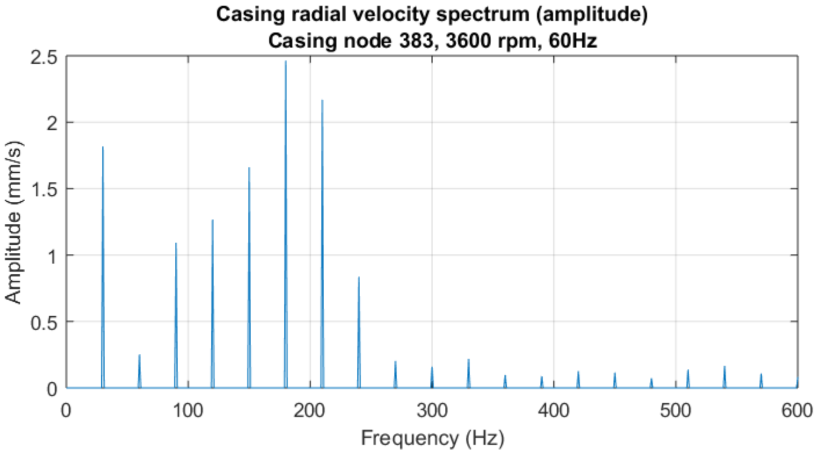

(b)

Figure 10. Periodograms of the steady-state casing signals. Light single-point rub. Low-band details. (**a**) Casing acceleration. (**b**) Casing velocity. For simplicity only the low-band side of the spectra—between zero and 600 Hz—is shown.

3.0.2. Real Cepstrum

The cepstrum analysis of the downsampled and filtered acceleration and velocity signals (Figure 11) underlines the rotor–casing impact frequency of 15 Hz—represented on the cepstra as impulse trains of quefrency 0.033 s—. Both cepstra are qualitatively and quantitatively very similar, although the velocity cepstrum looks coarser due to the lower sampling frequency of the downsampled velocity data.

Peer-reviewed version available at *Sensors* **2018**, *18*, 1931; doi:10.3390/s18061931

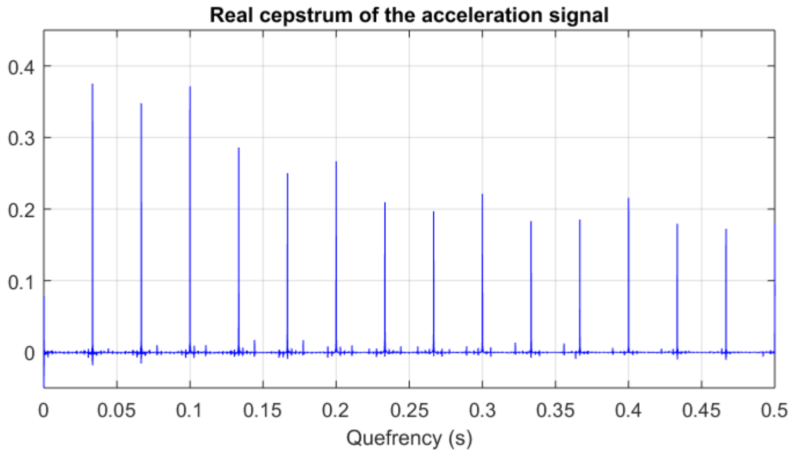

(a)

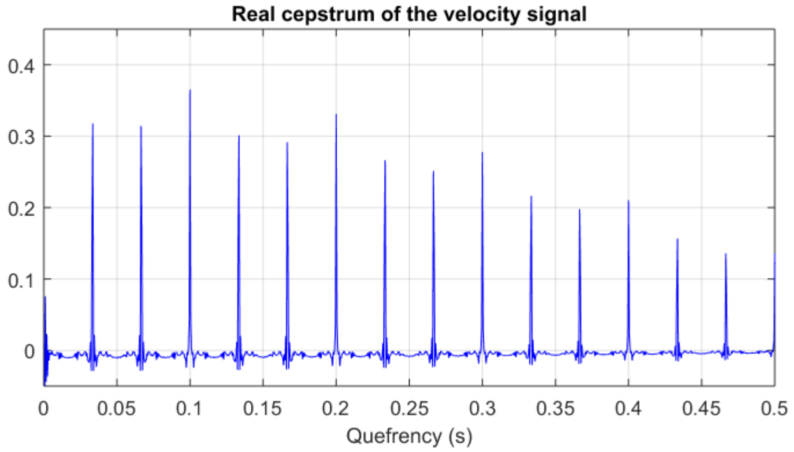

(b)

Figure 11. Real cepstra of the accelerometer signals. Light single-point rub. (**a**) Acceleration signal. (**b**) Velocity signal.

3.0.3. Continuous Wavelet Transform

The acceleration and velocity data was decomposed into wavelet coefficients with the Morlet wavelet function. Close-ups of the acceleration and velocity scalograms representing coefficient absolute values with a colored scale are shown in Figure 12.

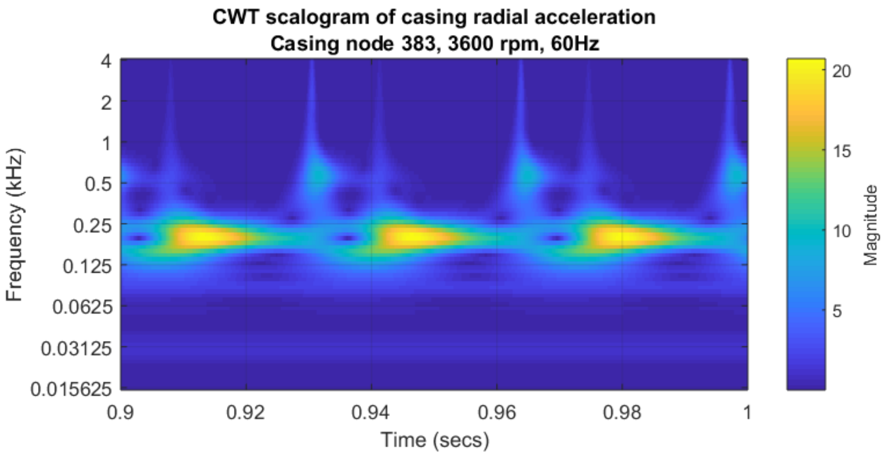

(a)

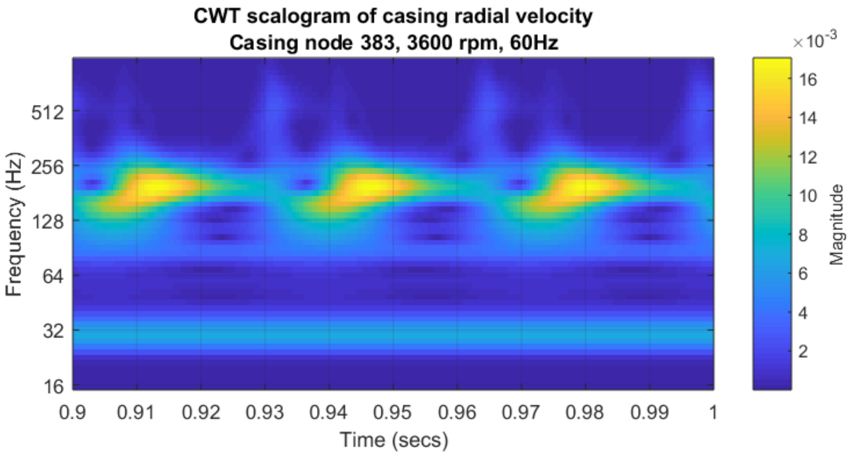

(b)

Figure 12. Details of the CWT scalograms of the steady-state casing signals with the Morlet wavelet. Light single-point rub. (**a**) Casing acceleration. (**b**) Casing velocity.

The scalograms of the acceleration and velocity records clearly highlight the excitation of the 200 Hz free vibration mode after the rub event; but most importantly, they disclose the short-lived free vibration transients of the high-frequency rotor and casing vibration, in the 0.3–4 kHz band, excited at the beginning and end of each rotor–casing contact, features that the Fourier-based methods failed to target. The velocity sampling vector contains more information of the low-frequency band of the spectrum, including the 30 Hz rotor–casing impact fundamental frequency and some of its harmonics, with the exception of the syncronous—60 Hz—unbalance-related harmonic, which lies buried under the rub features. Most of the high-frequency information in the acceleration data vanishes when this is time-integrated and downsampled but some of is still distinguishable.

4. Discussion

In this work we have presented a model of an aeroderivative gas turbine for the simulation of abnormal duty. In particular, it succeeds in reproducing a common type of rub encountered in conventional turbomachinery, the partial single-point rub [23].

This rub reflects on the casing acceleration and velocity signals as impulse trains (Figure 9), each impulse marking the beginning or the end of rotor–casing contact. Since each one of those sharp peaks supposes a perturbation of the casing, they are followed by transient oscillations containing a number of rotor and casing vibration modes, the most notorous of them being the rigid solid casing mode: the lowest of all the casing natural modes (Figure 5c). Those oscillations would fade in the course of time as a result of damping.

The Fourier spectra of the signals are mainly comprised of impulse trains with fundamental frequency equal to the impact frequency: half the rotor rotation speed (Figure 10). The highest impulse harmonics in the spectra are the 30 Hz harmonic—in the velocity spectrum—and the harmonics closest to the 200 Hz casing mode. The periodicity of the rub-related impulse train is evidenced by the cepstra as another train of impulses (Figure 11).

The Fourier spectra and the cepstra in Figures 10 and 11, due to the small frequency resolution—0.5 Hz—, fail to make visible the high-band rotor and casing transient modes excited by the rub perturbation. This elements can instead be identified and precisely localized in time with the application of the Continuous Wavelet Transform on the signals (Figure 12). Because of the very large time resolution of the CWT at high frequencies, the analysis of a short vector of acceleration samples containing just one of the rotor–casing impacts suffices to confirm the presence of those high-frequency and brief vibration transients and to localize them at the two ends of each rotor–casing contact, confirming the existence of rotor–casing rub. The CWT scalograms of the velocity data are better suited to visualize the low-frequency features of the rotor–casing rub, including the fundamental rub frequency band some of its low-band multiples.

The visualization of the evidences of rotor–casing rub on a Fourier spectrum would require to collect very large sampling vectors with large time intervals between the first and the last sample—to improve frequency resolution as much as needed without worsening the spectrum frequency range—. Such data recollection consumes great computational resources and necessitates a time span in which many impacts between rotor and stator may take place before its final detection. On the other hand, the Continuous Wavelet Transform has the potential to identify rotor–casing rub with the analysis of only one impact in a very short time span, thus enabling the early detection of this malfunction.

Conflicts of Interest: The authors declare no conflict of interest. Despite the technical support brought by GE this research received no sponsoring.

References

1. Muszynska, A. *Rotordynamics*; CRC Press: Boca Ratón, Florida, USA, 2003; ISBN 9780824723996.
2. Bently, D. E.; Hatch, C. T. *Fundamentals of Rotating Machinery Diagnostics*; Bently Pressurized Bearing Press: Minden, Nevada, USA, 2002; ISBN 978-0971408104.
3. Chen, G. Characteristics analysis of blade-casing rubbing based on casing vibration acceleration. *Journal of Mechanical Science and Technology* **2015**, *29*(4), 1513-1526.
4. Chen, G. Study on the recognition of aero-engine blade-casing rubbing fault based on the casing vibration acceleration. *Measurement* **2015**, *65*, 71-80.
5. Yu, M.; Jiang, G.; & Wang, W. Aero-engine rotor-static rubbing characteristic analysis based on casing acceleration signal. *Journal of Vibroengineering* **2015**, *17*(8), 4180-4192.
6. Chen, G. Simulation of casing vibration resulting from blade-casing rubbing and its verifications. *Measurement* **2016**, *361*, 190-209.
7. Chen, G. Vibration modelling and verifications for whole aero-engine. *Journal of Sound and Vibration* **2015**, *349*, 163-176.
8. Wang, N. F.; Jiang, D. X.; & Han, T. Dynamic characteristics of rotor system and rub-impact fault feature research based on casing acceleration. *Journal of Vibroengineering* **2016**, *18*(3), 1525-1539.
9. Randall, R. B. A history of cepstrum analysis and its application to mechanical problems. *Mechanical Systems and Signal Processing* **2017**, *97*, 3-19.
10. Kovacevic, J.; Goyal, V. K.; & Vetterli, M. (2013) Fourier and Wavelet Signal Processing. Chapter 6, section 5. Available online: http://www.fourierandwavelets.org/ (accessed on 28 December 2017).
11. Yan, R; Gao, R. X.; & Chen, X. Wavelets for fault diagnosis of rotary machines: A review with applications. *Signal processing* **2014**, *96*, 1-15.

Peer-reviewed version available at *Sensors* **2018**, *18*, 1931; doi:10.3390/s18061931

12. Yang, Y.; Cao, D.; Yu, T.; Wang, D.; & Li, C. Prediction of dynamic characteristics of a dual-rotor system with fixed point rubbing—theoretical analysis and experimental study. *International Journal of Mechanical Sciences* **2016**, *115*, 253-261.
13. Jones, S. Finite elements for the analysis of rotor-dynamic systems that include gyroscopic systems. *Doctoral dissertation, Brunel University* **2005**.
14. Muszynska, A. *Rotordynamics*; CRC Press: Boca Ratón, Florida, USA, 2003; Chapter 3, section 6.1, ISBN 9780824723996.
15. Ahmad, S.; Irons, B. M.; & Zienkiewicz, O. C. Analysis of thick and thin shell structures by curved finite elements. *International Journal for Numerical Methods in Engineering* **1970**, *2*(3), 419-451.
16. Bently, D. E.; Hatch, C. T. *Fundamentals of Rotating Machinery Diagnostics*; Bently Pressurized Bearing Press: Minden, Nevada, USA, 2002; Chapter 18, ISBN 978-0971408104.
17. Bently, D. E.; Hatch, C. T. *Fundamentals of Rotating Machinery Diagnostics*; Bently Pressurized Bearing Press: Minden, Nevada, USA, 2002; Chapter 2, ISBN 978-0971408104.
18. Craig, R.; & Bampton, M. Coupling of substructures for dynamic analyses. *AIAA journal* **1968**, *6*(7), 1313-1319.
19. Newmark, N. M. A method of computation for structural mechanics. *Journal of the engineering mechanics division* **1959**, *85*(3), 67-94.
20. Vetterli, M.; Kovačević, J.; & Goyal, V. K. *Foundations of Signal Processing*; Cambridge University Press: Cambridge, UK, 2014; Chapter 3, section 4, ISBN 978-1107038608.
21. Cooley, J. W.; & Tukey, J. W. An algorithm for the machine calculation of complex Fourier series. *Mathematics of Computation* **1965**, *19*(3), 297-301.
22. Littrell, N. Selecting the right sensors for your machine *Orbit Magazine* **2013**, *33*(1), 46-53.
23. Bently, D. E.; Hatch, C. T. *Fundamentals of Rotating Machinery Diagnostics*; Bently Pressurized Bearing Press: Minden, Nevada, USA, 2002; Chapter 2, ISBN 978-0971408104.
24. Lin, J.; & Qu, L. Feature extraction based on Morlet wavelet and its application for mechanical fault diagnosis. *Journal of sound and vibration* **2000**, *234*(1), 135-148.
25. Zheng, H.; Li, Z.; & Chen, X. Gear fault diagnosis based on continuous wavelet transform. *Mechanical systems and signal processing* **2002**, *16*(2-3), 447-457.
26. Wu, J. D.; & Chen, J. C. Continuous wavelet transform technique for fault signal diagnosis of internal combustion engines. *NDT & E International* **2006**, *39*(4), 304-311.
27. Rafiee, J.; Rafiee, M. A.; & Tse, P. W. Application of mother wavelet functions for automatic gear and bearing fault diagnosis. *Expert Systems with Applications* **2010**, *37*(6), 4568-4579.
28. Su, W.; Wang, F.; Zhu, H.; Zhang, Z.; & Guo, Z. Rolling element bearing faults diagnosis based on optimal Morlet wavelet filter and autocorrelation enhancement. *Mechanical systems and signal processing* **2010**, *25*(5), 1458-1472.
29. Tang, B.; Liu, W.; & Song, T. Wind turbine fault diagnosis based on Morlet wavelet transformation and Wigner-Ville distribution. *Renewable Energy* **2010**, *35*(12), 2862-2866.
30. Kankar, P. K.; Sharma, S. C.; & Harsha, S. P. Fault diagnosis of ball bearings using continuous wavelet transform. *Applied Soft Computing* **2011**, *11*(2), 2300-2312.
31. Bently, D. E.; Hatch, C. T. *Fundamentals of Rotating Machinery Diagnostics*; Bently Pressurized Bearing Press: Minden, Nevada, USA, 2002; Chapter 8, ISBN 978-0971408104.
32. Ashmead, J. Morlet wavelets in quantum mechanics. *Quanta* **2012**, *1*, 58-70.